ERASMUS MUNDUS MASTER IN
MEMBRANE ENGINEERING
FOR A SUSTAINABLE WORLD
EM3E-4SW

With the support of the
Erasmus+ Programme
of the European Union

Membrane surface nanopatterning: state of the art and perspectives in membrane applications involving light

Dissertation for obtaining the Master degree in Membrane Engineering

Erasmus Mundus Master in Membrane Engineering for a Sustainable World

Astghik TSOKOLAKYAN

15th of July 2020

Universidad de Zaragoza

Supervisor: Dr. Reyes Mallada

www.em3e-4sw.eu
em3e-4sw-project@umontpellier.fr

The Erasmus Mundus Master in Membrane Engineering for a Sustainable Word (EM3E-4SW) is an education programme financed by the European Commission - Education, Audiovisual and Culture Executive Agency (EACEA), under Project Number-574441-EPP-1-2016-1-FR-EPPKA1-JMD-MOB. It is also supported by the European Membrane Society (EMS), the European Membrane House (EMH), and a large international network of industrial companies, research centers and universities.

Abstract

With the increasing search for sustainable and economically attractive technologies, surface patterning methods are getting broader range of industrial applications. In the scope of this research we discuss the role of surface patterning for the membrane performance and its improvement. We discuss the recent developments in the membrane surface patterning technologies as well and the influence of fabrication parameters on the outcome. This brings us new insight on the huge potential of surface patterning technologies. Finally, the experimental part is aimed to design and fabricate plasmonic nanostructures on the membrane surfaces, by using nanopatterning techniques. The plasmonic membranes with light trapping properties can be used as a solar thermal conversion cell in evaporation processes.

Contents

Introduction

This research focuses on micropatterning technologies and their importance in various membrane processes. As will be seen in the scope of the study, the membrane patterning has a considerable impact on the membrane performance. Membrane surface is defining many of the membrane properties, thus its modification is a promising way of gaining desired results. Membrane micropatterning or nanopatterning is a low cost and relatively fast alternatives to complex chemical treatments steps. As another advantage, the micropatterns can have a long-lasting impact on the surfaces, which eliminates the need for regular treatments.

In the first section we tackle the main issues in each membrane processes, and the way that micropatterning affects their performance. Membrane surface is the critical limiting factor for the membrane performances such as fouling, wetting, interfacial resistance. As we will see the micropatterning has a great potential to solve them.

Furthermore, in the next section we discuss the main nano- and micropatterning techniques, and mention their applicability in patterning of different membranes.

The initial focus of the studies was fabricating grating surfaces that will trap the visible light, and integrating it into membrane distillation system. Thus, the next part is detailed on the membrane distillation and solar thermal systems. In the last bibliographic part we discuss the plasmonic grating designs in terms of their thermal conversion properties and compare to other plasmonic nanostructures.

The experimental part includes preparation of the grating template and its characterization. The future work has been inferred from the results obtained during the current experiment.

1. Nano and micro-structured membranes in technology applications

1.1. Ultrafiltration and microfiltration

Ultrafiltration (UF) processes are used for cleaning liquids from colloids, viruses and proteins, while the microfiltration (MF) separates the suspended solids, bacteria and high molecular weight species. Both separations processes are based on size rejection, and the transport occurs by pressure-driven pore flow. The fouling in microfiltration and ultrafiltration occurs by two ways: pore clogging and surface cake layer formation.[1]. The flux resistance is mainly caused by the cake layer, which is formed by the particles that deposit on the surface.

Micro and nanopatterning of the membrane surfaces have improved the microfiltration and ultrafiltration performances. In UF membranes it has resulted in increased critical flux J_c, that is the maximum flux below which there is no fouling. After nanopatterning of the ultrafiltration membrane Jc has increased by 19-45% , when tested on silica particles rejection. [2] The J_c was enhanced with higher patterns, as the particle and bio-cell deposition on the higher ridges is mitigated with the higher shear stress. [3] [4][5] Even though there still is deposition in the valleys, where the shear stress is low, the average deposition on the nanopatterned surfaces is less compared to the flat ones[6]. The patterns enhanced both critical flux and the recovery rate after cleaning compared to the flat membranes. [7] [8].

At low Re numbers and velocities, the particle size to pattern size relation is important factor for fouling mitigation. For larger than 0.1µm particles the back diffusion is governed by shear forces

and and J_c increases with the size of the particle[3], [7]. The shear-induced diffusion is increasing with particle-to-pattern size ratio and the flow velocity, which lead to smaller accessible deposition area inside the patterns.[6] [9][[3][10][6]. At low Re numbers (< 1600) the size-based exclusion of the particles and graphoepitaxy on the pattern is the main mitigation mechanism [11]. Thus, both experiments and simulations are done to study the effect of the ratio of particle-to-pattern size on the membrane fouling [7], [8], [10]. Moreover, the patterns comparable to foulant sizes, can lead to ordered deposition or graphoepitaxy on the grooves and prevent the irreversible fouling. [12]. Moreover, the best value of particle to pitch ratio was found for minimum deposition rate, which vary with pattern shape and the interaction between the foulants and the surface [13]. The bio-foulants have more complex interactions highly depending on the length scale of the patterns on the surface, which has been reviewed by Cheng et.al.. [14].

At higher Re numbers (higher than 1600) and velocities, the patterns induce high turbulence depending, with the efficiency depending on the shape and size. The vortexes formed at high Re numbers (high velocities), can remove more particles from the valleys of the patterns, for the larger spacing of the peaks(Figure 1). With a larger area of the vortex the particles can access the high drag flow region easier [9]. The propogation stream at the 90^o angle in respect to the pattern direction resulted in minimal deposition.[3].

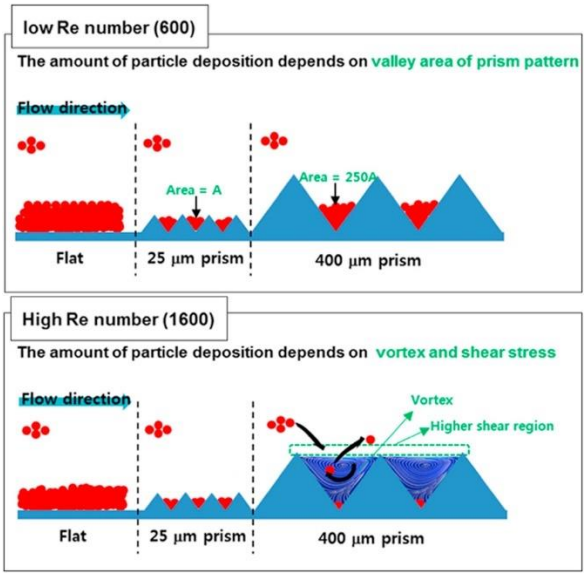

Figure 1: Summary of the particle fouling mechanisms at low (Re=600)and high (Re=1600) Re numbers

The main impact of nanopatterning on the filtration process is summarized in Figure 1. At low Re numbers and velocities, the increase of particle sizes to a certain value, as well as higher patterns

can prevent the fouling of the surface. While at the increasing Re numbers and velocities, larger patterns and their shapes (aspect ratio) are generating vortex and shear stress, which is the main way for reversing the fouling.

Table 1: Summary of results from using micropatterned membranes in the particle filtration

Application	Fabrication method	Feature size Patterns (h/w/p)	Main results	Reference
MF	PSmM	Prism h/w (nm) 4-7nm/ 42-48nm 13-15nm/4550nm 18-20nm/50nm	Larger patterns result in higher flux and less fouling by biocells, due to high surface arsea and higher local shear stress near the apex. Flux improved by 50%.	[12]
MF	NIL	Nano-Pillars P=575nm (1:1) L_1 = 50nm AR =1.15 H:150-170nm AR = 3.83 P2P = 250/575 = 0.5 P2P = 500/575 = 1.	The patterned membrane increased the critical flux for 30% and 40% for 0.25 µm and 0.5 µm size patterns. The sharper and higher patterns induce higher shear rate near the membrane surface. Particles with diameter of 0.5µm particles showed less fouling and were closest to the half size of pattern trench. 41% lower fouling rate. dJ/d(TMP). Crossflow velocity is 0.03m/s.	[2]
UF	NIL	Nano-pillars Pitch-834nm Ratio 1:1 100-120nm AR = 8	19–45% increase in the apparent critical flux, with the magnitude dependent on particle size. The crossflow velocity is 0.06 m/s.	[3]
UF	NIL	L (h): 100–120 nm	45% increase in flux recovery ratio and 91% increase in permeate flux during bovine serum albumin/phosphate buffered saline filtration	[7]
UF	NIL	Hexagonal packing array [nm] Nano- d/h = 100/100nm Micro- d/h = 2000 /2000nm	The deposition has it's minimum deposition value at Particle size/pattern size = 3 value for both mono-disperse and poly-disperse mixtures 50% less deposition (mg/m^{-2}).	[10]
MF	CFD calculations	h/w/spasing [µm] A: 25/25/0 B: 400/400/0 C: 400/400/400 D: 400/400/800	Larger patterns were successful in high Re numbers since the vortex region is closer to the apex. The increase in interval resulted in less deposition, the deposited mass ~ (vortex/permeation) stream areas. 40% -47% improvement without spacers for 25um and 400um and 87% less deposition (in mg) for 400um spacing.	[9]

MF	PSmM	pyramid 8.2-9.9 µm height	After 60h of testing the biocells fouling raised TMP of the flat membrane to 20kPa, while the TMP of the patterned membrane remained the same.	[15]
Table Included from [16]				
Particle filtration	TEM (R2R-NIL)	L (w/p/h): 389/545/72 nm	10 times larger surface area successfully nanoscale patterned, aligned deposition of silica particles	
	PSmM + float casting	Pore (d): 80–240 nm (microsieves)	>99% rejection for particles with 330 nm diameter	
	PSmM	Pore (d): 2–5 mm (microsieves)	Stable flux operation with backpulsing during MF of protein solutions	
Water/wastewater treatment	PSmM	Py (w/l/h): 25/25/16 mm	29–44% increase in pure water permeability up to _60% less particle deposition	
	PSmM	Pr (w/h): 33–45/4–18 mm	~20% increase in water flux, no change in TMP (3_ less than pristine membrane) during activated sludge MF	
	PSmM	Hollow fiber Pr (w/h): 28/10 mm	Bioreactor: 20–25% higher water flux (activated sludge). 30 kPa TMP reached in 29 hours with Pr-patterned compared to 7 hours with non-patterned membrane	
	PSmM	L (w/p/h): 20/85/22 mm	Decrease in fouling rate for patterned membranes during crossflow filtration of yeast suspensions	

1.2. Reverse Osmosis and Nanofiltration

Reverse osmosis, pervaporation and polymeric gas separation membranes have dense polymeric structure, and the transport is based on solution diffusion mechanism. RO membranes are used for desalination and deionization of water, including monovalent ions. Nanofiltration membranes are the intermediates between the reverse osmosis and ultrafiltration membranes, as the pore diameters lie between 5A and 10 A. The separation by nanofiltration is in the transition region between pore flow and solution-diffusion mechanism, thus it rejects the most organic solutes and multivalent ions, but may pass monovalent ions.[1] Regardless of the separation mechanism these membranes are highly prone to fouling by colloids and bio-foulants [17] [18][19].

The main factor impacting the particle deposition is the surface morphology of the RO and NF membranes. High roughness of the selective layer promotes clogging of the membrane by the particles, which results in rapid loss in flux.[20][17][21]. The flux declined in proportion to the mean roughness of the membranes in experiment conducted by Li et al.[18] [17] Moreover the

Application	Modification	Surface roughness(rms) Patterns (h/w/p)	Main results	References
RO	-	rms Cm = 300nm CAm ~ 10nm	Composite membrane(C_m) suffered higher fouling and thus higher flux decline of 50% while the CA membrane declined or only 10% during initial 12h of filtration.	[17]
RO	-	rms 10.1nm 33.4nm 43.3nm 52.0nm	The membranes exhibited higher fouling rates by the same order of their roughness. Thus the roughest membrane was the most fouled.	[20]
RO	-	Rms 70±5.8 nm 70±4.4 nm 123±9.6 nm 58±3.6 nm 43±0.1 nm	The membrane with rms of ~123nm showed 2 times flux decline rate than the rest, having ~1.6 times higher roughness, thus the former is directly related to the surface roughness. The membrane with sharper peaks showed less flux decline.	[18]
NF	NIL	h/p/w= -180/625/303 nm	The patterning of the membrane resulted in fouling rate decline and threshold values increase by 25% for all types of the foulants.	[22]
NF	NIL	Pristine =240nm Pressed rms = 75nm Patterned rms = 170nm d/p/w = 230/625/300nm	The patterning and pressing mitigated the fouling of the membrane from 22% decline to 8% flux decline, respectively, through decreasing the roughness in both cases. Patterning resulted in reduced drop in the flux, due to adding ordered roughness, which disrupted the hydrodynamic boundary layer during flow over the membrane.	[23]
NF	NIL	Patterned: d/p/w = ~30/575/210 nm	NIL-imprinted TFC membrane declines to 82% 10 times sower of their initial permeance , than the flat_TFC. The patterned membrane recovered 25% more of their initial permeance compared to the flat TFC.	[24]
NF	NIL and IP	32x15 and 3µm parallel grooves	50% improvement in relative flux over 100ml permeate volume in dead-end filtration ~3um cake layer vs 1,1um flat equivalent	[25]

fouling rate was lower for the membrane with sharper peaks but the same roughness.

In contrast, the patterning of the membranes have improved the membrane performance by adding ordered roughness to the surface. The latter causes selective deposition of the colloids, which is less favourable than deposition on the flat membrane [25], To prove this Weinmann et al. [23] both, pressed and thermally embossed line ad groove nano-patterns on the Polyamide

TFC membranes. The flux decline was alleviated from 22% for pristine the TFC to 8% for embossed membranes, due to the declined surface roughness. The patterned membrane fouled slightly slower than pressed one, which was attributed to the presence of the patterns. Embossing nanopatterns of TFC membranes resulted in 10 times slower flux decline and 25% higher recovery, than that of unpatterned membranes[24]. Nanopatterns have increased critical flux. [22], [26], [27] [21]. The patterns not only increase the surface area and but also induce turbulence at the surface thus inhibiting fouling.

The experiments prove that the roughness of the surface can either enhance or mitigate the fouling., which depends on the shape, sizes, regularity and even direction towards the pores of the membrane.

1.3. Proton exchange membranes

Proton exchange membranes, also known as polymer electrolyte membranes are integrated into Polymer electrolyte membrane fuel cells (PEMFC) are used in Membrane electrode assemblies. In the proton exchange fuel cell is the membrane is carrier for protons and a barrier for reactants and electrons. The Nafion membranes are used for their high proton conductivity and chemical stability. The geometry and morphology of the PEM and catalyst interface (PEM|CL) have major impact on performance and improvement of Peak power density, high frequency resistance/ohmic resistance, ECSA (electrochemically active surface area), low frequency resistance/mass transfer resistance of the PEMFC [28].

In general, micropatterning increased the surface area of the PEM|CL interface, and improved the power density and charge transfer resistance linearly.

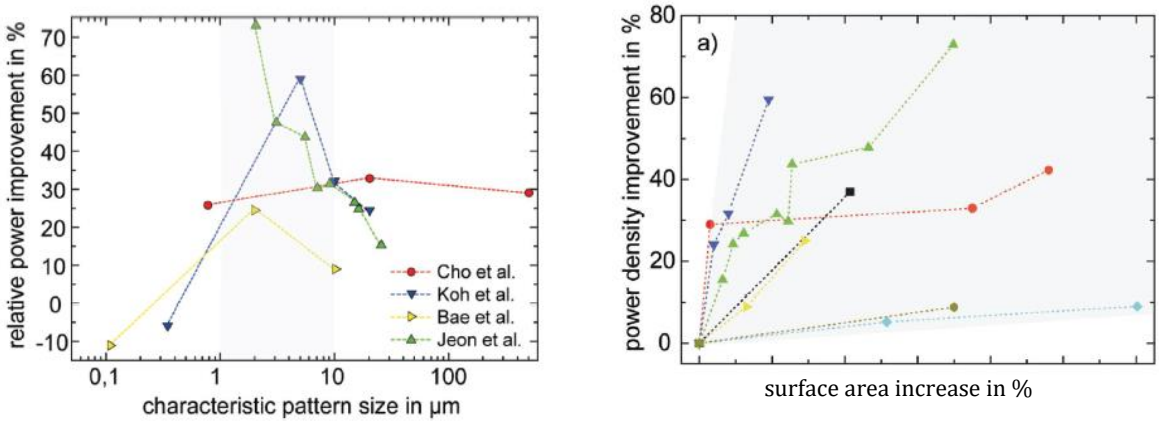

Figure 2: relative power improvement with the patterned membrane size b) Power density improvement with surface area increase of the membrane [29]

Although the nanopatterns provide a higher surface area than the micropatterns, the increasing trend was only valid for micropatterns down to 1-10µm sizes., as can be seen from the change in trend at the transition from the micropatterns to nanopatterns in the Figure 2a. This was attributed to the weak contact between nanopatterns of the membrane and catalyst layer.

The mass transport is one of the crucial factors in PEM performance. At higher current densities (approx. 0.2 A cm^{-2} a) more than 50% of the power density [30] improvement depends on the mass transfer limitations. They are caused by insufficient water management (at high current densities more water is produced) resulting in lower oxygen diffusivity. The surface patterning of the interface improves the mass transfer at the three-phase boundary of pore space, electrode and electrolyte mainly in the cathode catalyst side.

The patterning resulted in improved kinetic performance as the enhanced electrochemically active surface (ECSA) together with more efficient oxygen conducting pathways effect in greater Oxygen reduction reaction (ORR) region [31], [32]. Enhanced oxygen diffusion and ORR activity result in more efficient Pt power utilization [16] . The ohmic resistance is governed by ionic conductivity and electrode/membrane interfacial resistance, and the charge transfer resistance is dependent on ORR activity [33]. Thus both the resistivities were improved from surface patterning. The improvements of water management, enhanced Pt-utilization and reduced ionic interface were more prominent at low Pt-loading values (<0.120.4 mg cm^{-2}).

Regarding the shapes of the patterns, prism-shapes have provided the best results, in terms of gas supply efficiency and prevention of flooding by water [30]. Reverse electrodialysis simulations by

CFD modelling showed that pumping power consumed for corrugated membrane was less than the flat membrane with spacer. [29]

1.4. Gas Separation and Pervaporation

Gas separation and pervaporation are gas/gas and liquid/gas separation processes, respectively. The gas separation is driven by the partial pressure gradient across the membrane and the pervaporation is driven by vapor pressure difference. The membranes used in pervaporation are dense and permeate compounds in vapour phase based on chemical potential gradient. Micropatterning of membranes increases the surface area, thus result in higher vapor and gas fluxes and pervaporation.

For membrane-based gas permeation and separation processes, fouling is not generally a concern because of the absence of a boundary layer. Therefore, the focus of surface-patterning in such applications is improvement of the permeate flux. Limited studies show that surface patterning of the membranes can significantly improve the permeation flux during gas permeation, pervaporation, and other gas–liquid contacting processes.

Pervaporation performance was enhanced by micropatterning, mainly due to increased surface area and promotion of microturbulence at the surface. The sub-micron line patterns (350-500nm high) have increased the flux by 14%, 10% of which was attributed to the increased surface area and 10% to the improved mass transfer of hexyl acetate solute [34]. Micrometer sized patterns on PDMS resulted in 2.11 times higher ethanol recovery, due to the higher flux through enhanced surface area [35]. In gas liquid-contactors, the sinusoidally hollow fiber membranes showed reduced diffusional resistance, due to secondary vortices at the surface as well as induced slip flow at the gas-liquid interface which mitigated the wetting of the surface[36].

Gas separation membranes with micrometer patterns showed 59% improvement in flux, which was related to enhanced lateral gas diffusion through the micro-patterns, with no impact of enhanced surface area [37]. On the other hand, increasing the roughness (86μm) of the film (<10μm), has decreased the surface resistance to gas permeation, which led to 2.4 fold higher flux and improved selectivity. The details from the studies are summarized in Table 2.

Table 2: Previous results from Gas separation membranes patterning adopted from [11]

Separation process	Fabrication Method	Feature Size	Main results	
Gas Permeation	Solution casting	L (w/p/h): 30/50/25 mm	Diffusive gas flux increase up to 59%.	[37]
Gas separation	Solution casting	Rms = 86μm corrugated on both sides	2.4 fold higher flux and improved selectivity	[38]
Pervaporation	UV radiation + periodic extensional elongation	L (w/p/h): 10 mm/16 mm/350–500 nm	Solute (hexyl acetate) recovery by organophilic pervaporation: 14% increase in solute flux	[34]
Pervaporation	Phase separation of PVDF and solution casting of PDMS	L(w/h) ~200/3.78 μm	2.11 times higher than the non-patterned one due to increased Surface area.	[35]

2. Patterning methods

This section discusses the recent micro- nano- patterning techniques that can be applied in nano-structuration of the membrane surface. From the top-down approaches we discuss template based micromolding and nanoimprint lithography. We also discuss the main principles and recent updates from bottom up patterning techniques recent updates related to ink-jet and 3D imprinting, block copolymer self-assembly. The techniques are summarized in the scheme below.

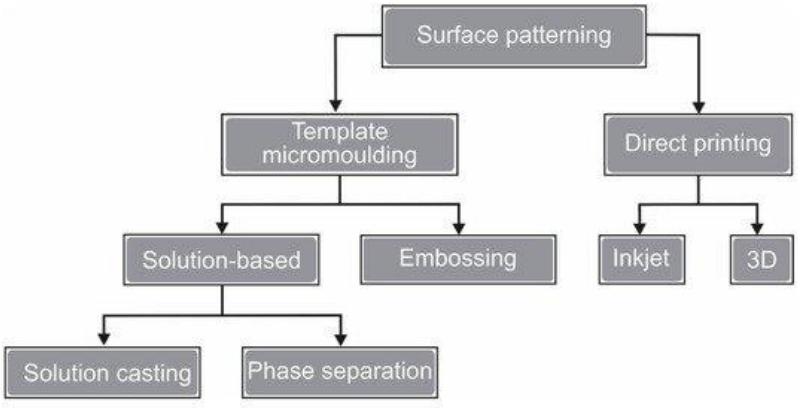

Figure 3: The schematic picture of the polymer nanopatterning techniques [39]

2.1. Template-Based Micromolding

The template-based micromolding use molds as template for shaping the materials, where the mold is the positive shape and the material takes the negative shape. Solution-based micromolding and embossing belong to template micromolding techniques.

2.1.1. Solution Casting Micromolding

Solution-based micro-molding is one of the two solution-based micromolding techniques. It is simply done by casting the polymer solution onto the mold. The polymer matrix is formed after the liquid evaporation, and has the negative shape of the mold. During the evaporation of the solvent, the membrane matrix shrinks, which creates a small gap between the mold and the polymer matrices that facilitates the demolding [39].

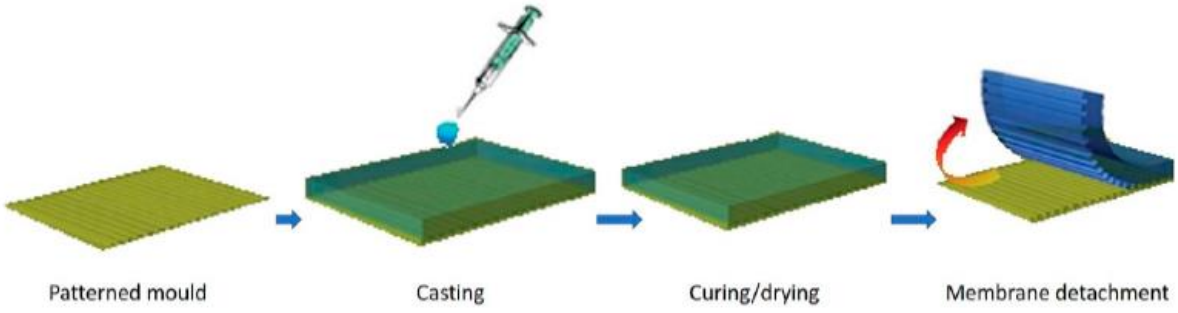

Figure 4. Solution casting micromolding procedure.[39]

This process is relatively fast and simple and can be done even at room temperature. After evaporation the solid membrane is carefully peeled of the master mold. It is widely used for PDMS and Nafion fabrication. [[39]].

The parameters controlling the outcome of the solution casting micromolding are solution viscosity, solution–mold interaction, solvent evaporation rate and adhesion of the casted polymer to the master-mold affecting the demolding process. The demolding results in rough polymer surfaces[[39]]. As mentioned before, the high roughness can cause fouling in the liquid separation processes such as RO, NF by creating boundary layer and enabling colloid particles accumulation on the surface. Therefore, the solution casting micromolding is mostly used in non-boundary

separation processes, e.g. PEM and MD. Particularly PEM the solution casting can be done by inkjet deposition or spray coating for thinner membrane layers [29].

2.1.2. Phase Separation Micromolding

Phase separation micromolding (PSmM) is also template-based micromolding technique. The process involves casting the solution on the template and immersing it in the coagulation bath with non-solvent, the latter causing the coagulation of the polymer (Figure 5). The process is usually called non-solvent induced phase separation(NIPS) [[39][40]].

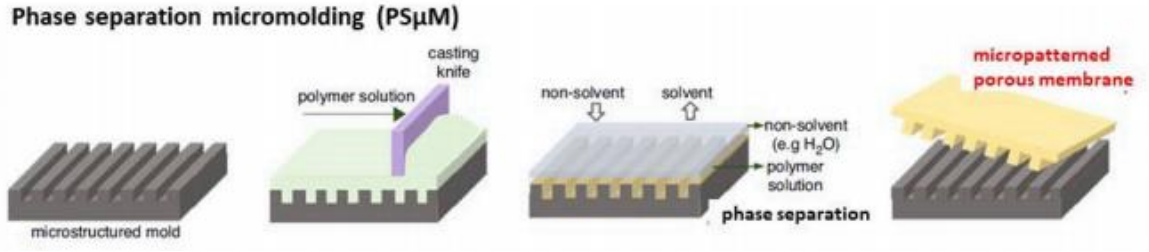

Figure 5: Phase separation micromolding schematic description. Reproduced from Heinz. Et al.[16]

The pore structure and the density of the membrane depend on the type of the polymer used and kinetics of the exchange [40]. The higher molecular weight and concentrations of the polymer result in denser structures. The fast exchange kinetics between solvent and non-solvent also results in skin layer formation. In order to slow down the solvent-non-solvent exchange, the membrane can be covered by spacer, or the solvent should have low miscibility with the non-solvent.

In this process the pattern is formed on the surface at the contact with the master mold. This alignment results in the formation of a dense skin layer on the patterned surface. The pattern is replicated only on the bottom side facing the mold. In case of the direct coagulation, the dense layer is usually formed on the mold interface. To form a pattern at the solvent-non solvent interface, the polymer is firstly exposed to non-solvent vapor, which leads to Vapor-induced phase separation (VIPS). The solution is then immersed into the non-solvent to form the final membrane matrix. [[39]].

The fast solvent exchange creates macro-voids in NIPS, with a dense layer on the top, and micro-voids below the skin layer. For VIPS, however the demixing is slower, which results in more rough

,thus more hydrophobic surface with larger mean pore size and higher pore size distribution. The average pore sizes of membranes can range from ~5nm-1µm for NIPS and the smallest of ~130nm for VIPS technique[11]. The VIPS kinetics was in-detail studies by Gencal, revealed that time of vapor exposure results in asymmetric pores and low polymer concentration for higher replication fidelity[41]. The replication fidelity of NIPS was closely studied by Won et. al. [5].
Combined NIPS and VIPS were employed in 2 layer MD[27][42] membranes and MF support [41] fabrication. The bottom support layer is made by NIPS for controlled pore sizes were made, and the top layer with patterns were made by VIPS, which also maximizes the hydrophobicity. Alternative fabrication of micro- nano- hierarchical architecture has been designed by combining immersion precipitation and rolling embossing. [43] The phase separation can also be temperature-induced, where the solvents change their solubility with temperature.

2.1.3. Thermal embossing

Thermal embossing or otherwise called Nanoimprint (NIL) or Microimprint (MIL) lithography transfer the patterns onto a flat membrane, by pressing it to the mold at high pressures and temperatures above the melting transition temperature T_g of the polymer. After release of the temperature polymer is going back to glassy state as the pressure is still applied. Thin porous polymers are patterned at lower than T_g or T_m to avoid pore -sealing and porous structure loss. In contrast to the dense polymers, the porous structure can be “imprinted” at lower temperatures than T_g and high pressures, as long as they are enough to plastically deform the membrane. The porous membranes deformation is based on bending of the pore walls. The plasticity is determined by the yield stress value(σ) of the membrane. The pattern height is linearly increasing with the pressure, above the σ value of the membrane. The bulging heights which determine the final pattern height on the membranes are generated by the plastic deformation in the linear-elastic region(Figure 7). Replication fidelity can be achieved by increasing the imprinting temperature and pressure, thus reducing the σ value.
MIL and NIL have been successfully used in UF support patterning. Maruf has studied the nanoimprinting conditions influence on the height of the patterns and determined the optimum

temperature and pressure for preventing PES membrane densification, which were 120°C, 40 bars and 3 mins (Figure 6,7).

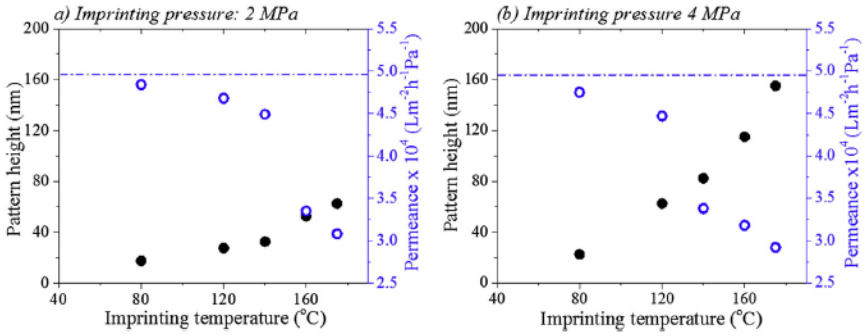

Figure 6: The influence of the imprinting conditions on the pattern height and permeance DI water permeance (pressed for 3mins) [44]

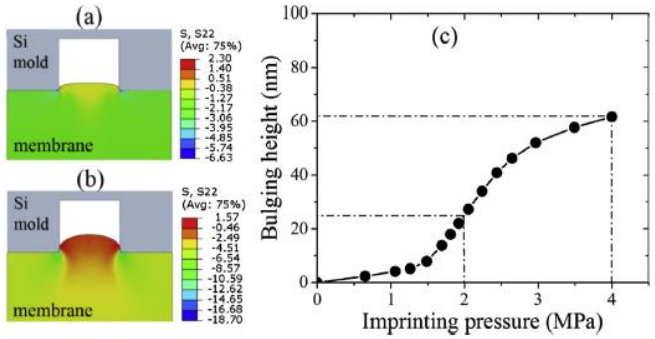

Figure 7: The pattern height fidelity depending on the applied pressure at 120°C, pressed for 3 mins [44]

In the summary of the used fabrication conditions (Table 1 Annex), the nanopatterns were achieved by applying 4 times higher pressure than the micropatterns.

The NIL patterning of the UF and RO membranes showed no difference in pore sizes after the patterning as well as the permeance or rejection values [45], [46]. However there were diverging views on patternability of the commercial TFC membranes. [26]. Previous studies summarized in Annex (Table 1) apply two different ways of TFC 1) UF support patterned by MIL and Interfacial polymerization (IP) of the upper layer (MIL_IP) 2) UF support fabricated by Phase inversion with selective PA layer deposited by interfacial polymerization (NIPS_IP) [21] [44], [47] 3) direct nanoimprinting on commercial TFC membrane.[26]. According to them NIPS_IP membranes had higher replication fidelity than the MIL_IP which could also be the reason for the better permeability and salt rejection values in the former samples [21]. Moreover, the micropatterning of the membranes have reduced boundary layer thickness and concentration polarization effect.

Generally, NIL patterning causes initial drop in permeance for most of the membranes, but is reduced less in the course of the filtration, due to initially pressing by NIL.

Porosity allows the patterning of the membranes at lower pressures and temperatures, as well as at faster rates than the bulk polymer. The scale-up of the TEM process is possible by Roll-to Roll process(R2R). The reduced contact time enables faster pattern transfer than TEM. Additionally, the imprinting cost of the porous membranes is reduced by the cooling/heating steps, as they maintain the plasticity at room temperatures[48].

2.2. Direct printing

2.2.1. Ink-jet printing

Ink-jet is performed by solution jet, which traces the pattern by droplet deposition on the surface. The pattern is formed after the evaporation of the droplets. It is usually used for chemical patterning of polymeric surfaces [11].

The pattern sizes can reach to nanometer ranges. The resolution of the patterns is higher in smaller droplet diameters, which is modified by viscoelasticity of the ink. The inkjet process have been integrated into IP of the selective layer on the support. Gao et. al. group fabricated membrane with alternating negative and positive channels, by depositing poly(allylamine hydrochloride) and poly(styrenesulfonate) inside the membrane pores with LbL inkjet printing. The selective charging of the track etched pores, enables high control over the permeating molecules and decreasing the chances of fouling (Gao et. al. 2016).

2.2.2. 3D printing

The 3D printing is based on Layer by layer (LbL) deposition of polymers, which is done by either photopolymerization, powder bed fusion, material extrusion and lamination. During the photopolymerization the photopolymers are cured along the trace of the laser[49].

The direct light processing (DLP) is a recent development to laser-induced polymerization which enables 25-100 times faster printing. The resolution for this technology is reported to be ~100nm, while the smaller details are made by other lithography techniques. 3D printing technology as well as the materials are reviewed by Low [50].

The 3D techniques are mainly used for membrane support fabrication followed by the deposition of the selective layer by interfacial polymerization or layer by layer techniques. The 3D printed supports have been effective in liquid filtration processes. The PES selective layer was vacuum-attached to 3D printed support, as a result the permeance was increased by 10%, and recovery rate with recovery rate increasing by 87%. Meanwhile for-gas liquid applications the PDMS membrane fabrication by direct DLP polymerization caused lower permeability, due to high crosslinking degree. Instead, the membranes made by filling the PDMS into the 3D printed sacrificial molds, based on the TPMS model, which, as simulated, performed better than the conventional PDMS hollow fiber membranes.

The advantages of 3D method over the NIL patterning, the possibility of patterning the membranes of complex shapes, such as hollow fibers. It is more sustainable as compared to PSμM in that there is no solvent needed here. It is highly suitable for high fabricating geometries with high precision, however are still limited by material choice, resolution and process upscaling.

3. Optical applications and nanostructured surfaces

3.1. Plasmonics and plasmonic nanostructures

There are two main plasmonic nanostructures actively used in light-harvesting technologies 1) plasmonic nanoparticles of different shapes (Ag, Au or Cu) 2) periodic grating on the metal/dielectric interface. Both of which interact with the light by different mechanisms.

Plasmonic metals Au, Ag or Cu, absorb the light photons at their resonant frequencies, this creates collective oscillation of the surface electrons, inducing Surface Plasmon Resonance (SPR). In case of nanoparticles, the absorbed electromagnetic field is localized around the nanoparticle, and dissipates in the proximity to it [51]. The absorption frequencies vary depending on the nanoparticle size and shape, the absorption ranges of Au nanostructures are summarized in (Figure 10).

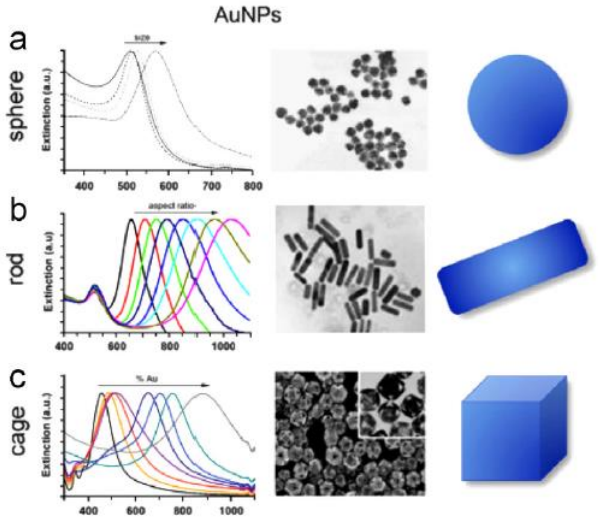

Figure 8: Plasmon resonance frequency range for AuNPs and AgNPs of sphere, rod, cage morphologies[52]

As can be seen from the figure, the absorption frequencies are falling into the visible light frequency range. However, nanoparticles absorb in a narrow light absorption band, and localize the heat in the proximity of the nanoparticle. In this aspect, the gold nanofilms may contribute to the homogeneous distribution at the surface, as the surface plasmons polaritons on the films can propogate to over 100μm.

Plasmon resonance on the grated metallic structures is caused by surface plasmon polaritons at the metal/dielectric interface, which couple with the light at the plasmon resonance frequency. The enhanced electromagnetic wave propagates along the interface and gets dissipated in the metal and dielectric media.

In order to induce SPR the incident light is increased by getting diffracted at the grated surface. The design of the periodic grating structures directly control the SPR resonant frequencies. Its spatial parameters are calculated by CFD modelling, based on the dispersion relation.

The in-plane wavenumber of the incident light the relation is :

$$k_x = k_0 sin\theta \quad (1)$$

Where k_x is the wavenumber on-plane direction and θ is the angle of the incident light.

To achieve the coupling the wavenumber of the incident light can be increased by the wavenumber of the periodical grating on the surface. In this case the wavenumber of the light is:

$$k_{sp} = k_x \pm m \cdot k_g \quad (2)$$

where m is the order and $|\vec{k_g}| = 2\pi / \lambda_g$,where the grating period λ_g should be the order of the incident light. wavenumber. In that case the k_{SP} periodic profile is coupling with the light in more than one allowed angles.

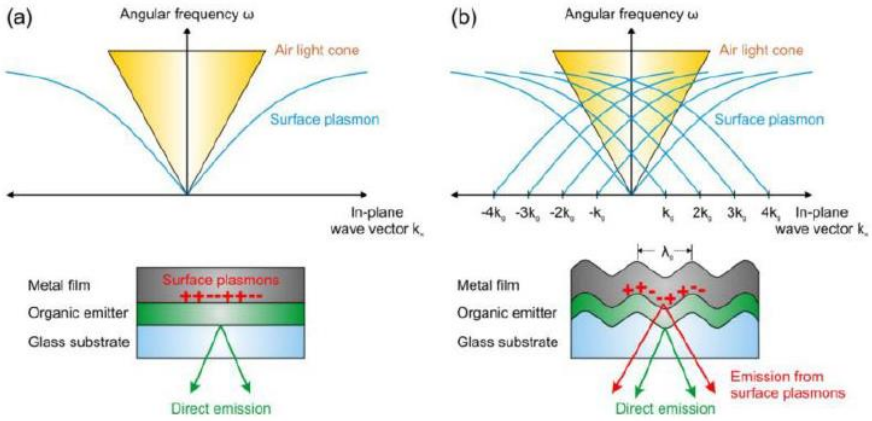

Figure 9: (a) Schematic illustration of dispersion of light and surface plasmons in a sample with planar interfaces. (b) Dispersion in a sample with periodically corrugated interfaces. In the latter case scattering of surface plasmons at the periodic grating may occur which shifts the SP wave vector by a multiple of the grating wave vector.[53]

The incident light has a parallel polarization (p-polarization). In the above system, by changing the incident angle we can get interference between different wavelengths of the incident light.

The advantages of the grated surfaces over the nanoparticles are that the resonating wavelengths can be tuned to the visible light ranges, which makes grating surfaces attractive for light harvesting applications. Moreover, as mentioned before, the energy is distributed at the interface of the membrane, over the long distances (>100μm for visible ranges). The disadvantages are dependence on polarization and angle of the incidence light. This leaves space for improvement of the designs combining the advantages of both nanostructures, which will be discussed in the next sections.

Our approach for designing light absorbing surface in the visible range was focused on fabricating plasmonic grated nanostructures on the membrane surfaces, by using surface nanopatterning techniques. In this section the study of the metallic grated design that has guided us is being discussed in more details.

3.1.1. Grated surfaces

In the experiment conducted by Sierant et. al. [54] suggested DVD grating as low-cost nanostructure for inducing SPR. DVD samples have been tested both experimentally and by modelling methods (RCWA and FDTD). The bare DVD metal grated samples and similar samples covered with 120 nm gold have been illuminated by laser beam (120mW) at wavelengths of 633, 785 and 1083 nm. The SPP efficiency was measured at different incident angles of the laser. The computed enhancement of the laser beam intensity at the modelled and real gratings of a DVD were: 50–60 times the intensity of the incident laser beam for 633 nm, 100–160 times for 1083 nm and 200–220 times for 785 nm (Figure 12).

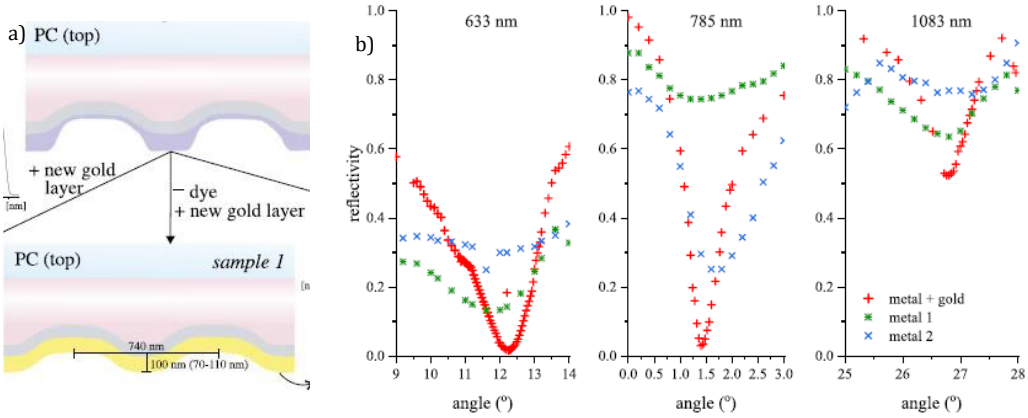

Figure 10: a) DVD samples bare metallic surface and metallic surface covered with gold b) The reflectivity of samples at varying angles of the laser beam (120mW). [54]

As shown in the Figure 12, among other samples the gold coated samples exhibited higher and sharper resonance peaks. Most importantly, the temperature measurements showed about 50% of

the laser beam power (90mW) is transformed to the heat due to plasmonic effects, with the temperature raise from 22°C to 70 °C (Figure 13).

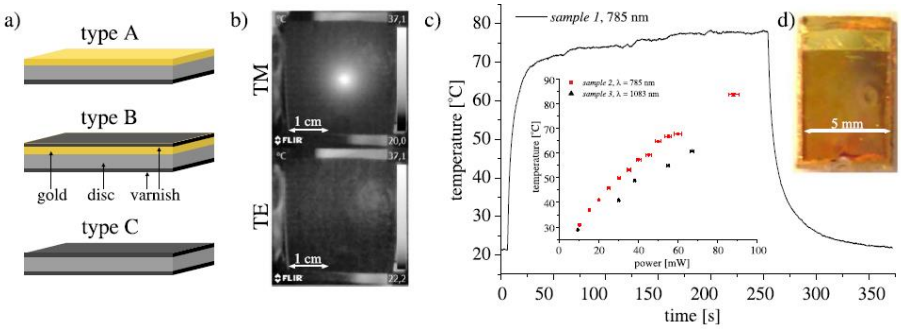

Figure 11: Description from the article [54] (a) Scheme of the samples used in thermoplasmonic measurements. Type A is a DVD+R sputtered with gold and covered with black matt varnish .Type B is sample 1 but covered with the varnish on the top side as well. Type C is the unmodified DVD covered with black matt varnish on both sides. (b) Typical temperature distribution obtained for SPPs presence (TM) and absence (TE).c) Typical temperature changes with time (90 mW, 780 nm) and laser power (inset). The error bars for the temperature are slightly smallerthan the size of the data point, (d) Example of sample 1 class with crater-like damage caused by 120 mW continuous laser beam.

Apart from knowing the mold structure, it is important to find the optimal thickness of the gold-coated layer, as too thick layer will act as an energy sink, and absorb the heat scattered from the plasmon resonance[55].

The results obtained in this experiment, namely the enhancement of the laser beam and the high conversion degree into thermal radiation inspired to test the DVD grating effect on the membrane surfaces.

3.2. Membrane applications activated by light

3.2.1. Membrane Distillation

Membrane distillation (MD) process separates two miscible liquids at different temperatures by microporous membrane. The driving force is the partial vapor pressure gradient from the temperature difference. The MD is used for water desalination processes. Its advantage over RO

process is that pressure difference is provided by heat, instead of pressure pumps, and has reduced sensitivity to the concentration polarization [1][56].

To overcome the major problems with fouling and wetting, surface corrugation have been employed in the MD membrane fabrication process (Khan et al., 2017; Kharraz et al., 2020).

Surface nanopatterning performed on the membrane mitigated the fouling and improved the flux through due to higher surface area and turbulence at the surface diminishing the temperature polarization[49]. The micropatterns were most effective in fouling prevention, as BSA deposition at the line patterns due to lower adhesion to the surface, which was also attributed BSA size being close to the pattern size[46]. As for the hollow fibers, micropatterns at the permeate side of MD membrane, higher flux can be achieved by increasing the cooling area at surface and disturbing the temperature polarization layer by the micro-turbulence, outer surface of the hollow fiber. García-Fernández et al. [59] obtained the highest DCMD permeate flux for hollow fibers, the improvement was observed only on the irregular patterns, while for the V shaped patterns higher than 30μm the higher permeate cooling couldn't compensate for the thicker TP boundary layer effect. Imprinting of millimetric patterns with spacer improved the flux by 27%, however didn't inhibit the wetting [42].

3.2.2. Improvement strategies

The abovementioned modifications are still not providing anti-wetting properties against high and low surface tension liquids. Anti-wetting properties of the surface are described by maintaining the Cassie state and the slippery state of liquid at the interface, at which the liquid is not touching the solid and flowing over solid-air-liquid interface. The flowing state is achieved by chemical modifications combined with patterning, which make the membrane superhydrophobic. However, it still can be wetted by low surface tension and non-polar oils. The hierarchical structures can maintain both states and prevent wetting by most of the liquids [57], [60]. This non-wetting interface is obtained by increasing the re-entrant states [61] (Figure 12).

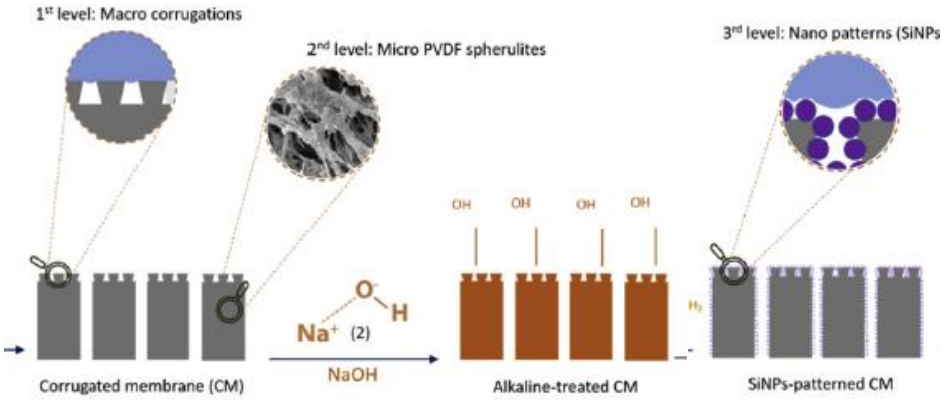

Figure 12: Fabrication of hierarchical PVDF membrane or MD [57]

The first re-entrant states were macro-corrugations. At this stage the micro-corrugations mainly increase membrane surface area (by 42%) and induce turbulence flow at the surface [15], [27]. Patterning of the PVDF composite membranes with diamond shaped spacer with millimetric dimensions results in ≈10 fold lower fouling rate [27], [60]. The second re-entrant state on the microns level is the rough and open structure on the surface, resulting from the fabrication method (VIPS in humidity created PVDF crystal spherulites). Kharraz et al. added vapour induced phase separation step to increase the roughness. The third re-entrant level was composed of sphere-shaped particles. This three-level hierarchical surface showed the best results in obtaining Cassier state factor <0.5 (created by SiNPs). The nano-structured surface was more slippery (SA< 3.8 º ± 1.3) compared to the micropatterned membrane (SA>22.4º ± 3.2). This resulted in more than 12h non-wetting behaviour for both oils(>200ppm), seawater and SDS. (> 1.0mM SDS).

3.3. Solar membrane distillation

Solar membrane distillation is using sunlight as a source of energy for evaporating the feed at the membrane surface. The main components for designing a light to heat generator are identified by Kim et al.[62] as 1) light absorber in broad wavelength range 2) insultation layer 3) porous system to let the water permeate through the membrane.

The absorbing material can either be carbon-based (Figure 9a), plasmonic or semiconductor. In case of plasmonic absorbers, the membranes are embedded with plasmonic nanoparticles, which

absorb the light and dissipate the heat in the surrounding media. Plasmonic materials have been extensively used for light to heat conversion in membrane distillation process (Figure 9b) [63].

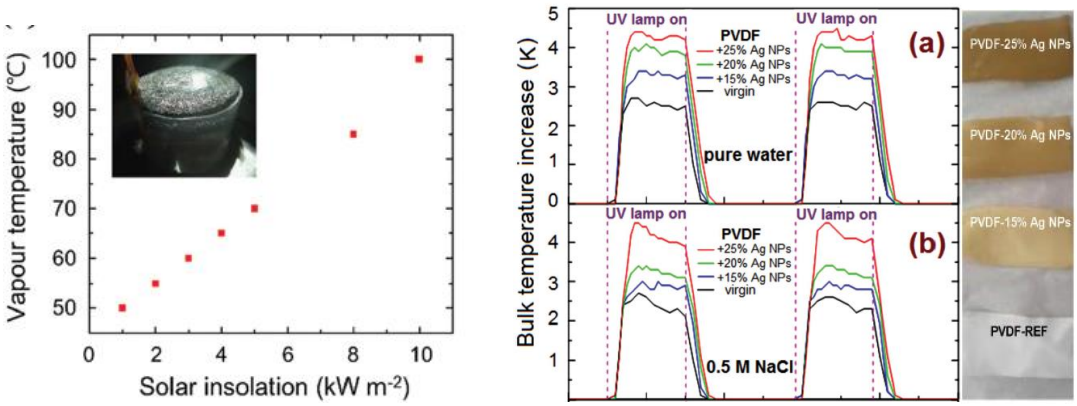

Figure 13: a) Vapour temperatures in carbon based solar evaporation system b) Bulk temperature increase of light Ag NPs embedded PVDF membrane under UV light [63]

4. Preliminary experiments on fabrication of nanostructured membranes by NIL

The experiment was aimed to fabricate periodic gratings sputtered with metal layer on the polymer membranes surfaces and test the light trapping and surface plasmon resonance effect on them.

In the experimental part of the project the following steps have been performed

1. DVD mold preprocessing and PDMS master mold preparation
2. Characterization of DVD mold and PDMS master mold by Scanning Electron Microscopy (SEM) and Atomic Force microscopy (AFM) techniques, the AFM measurements were done by tapping mode by using the tip CSG30

3. Hot embossing on Polyvinylidene fluoride (PVDF) membranes
4. Characterization of the imprinted membranes by SEM by ImageJ, AFM by Gwyddeon

4.1. Master mold preprocessing

The DVD+R and DVD-R of Verbatim brands have been split into top and bottom layers as described in the article [54] . The DVD layers have been separated by the azo dye section into top and bottom parts. Top part: Polycarbonate metallic and the transparent polycarbonate part has been cleaned from the azo dye layer with ethanol and dry nitrogen. DVD +R/-R composite layers are: the top Polycarbonate (PC) of 600um thickness, adhesive layer with surface (~50um), metal layer with of 40-100nm (Al or Al alloy), dye (~100um), recording layer (cyanine, phthalocyanine or metal azo) and the bottom PC layer(~600um).

4.2. PDMS stamp preparation

We followed the steps described by the paper mentioned above[54]. The target DVDs have been separated and 3 parts have been chosen.

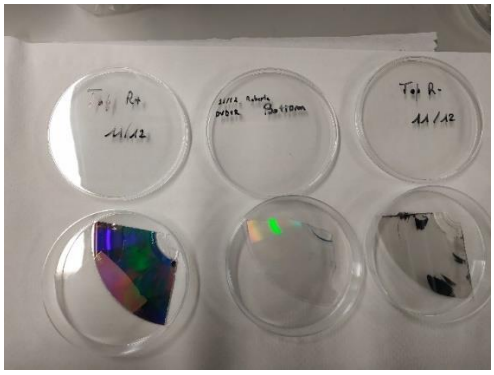

Figure 14: DVD+R top ; DVD+R bottom ; DVD-R bottom (from left to right)

After separation each of them have been washed with ethanol and dry nitrogen. The PDMS solution(SYLGARD^{TM} 184 Silicone Elastomer base) was mixed with the curing agent with ratio of 7.5:1 and poured on the DVD surfaces after degasifying in the vacuum desiccator.
The samples have been cured in the oven at 80°C for at least 2hours.

4.3. SEM and AFM characterizations of DVD and PDMS replica

The surface topography of DVD+R has been measured by SEM inspect microscope. Figure 15 shows the well-defined and uniform periodical gratings for the top DVD parts.

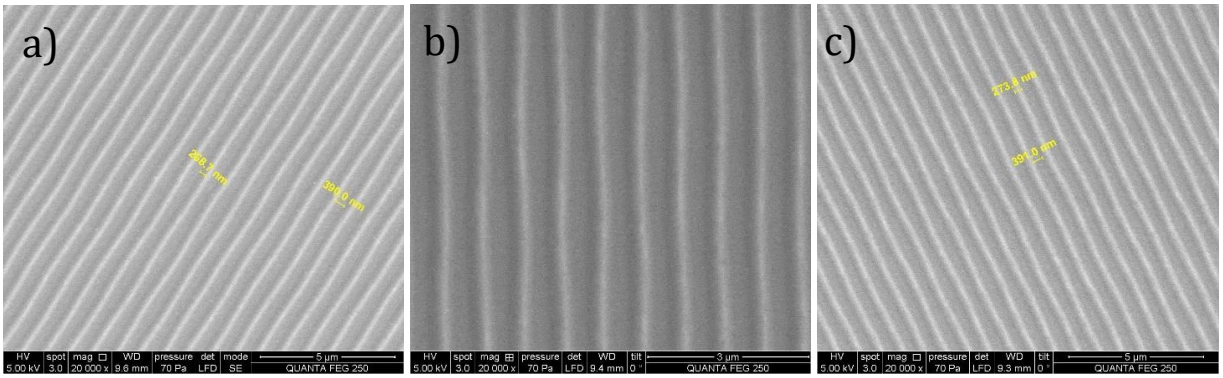

Figure 15: DVD+R top parts: a) no azo b) and c) with azo

The measured dimensions for the DVD +R surface gratings are presented in the Table 5,6,7 (Annex). The depth of the DVD gratings has been measured by AFM. The DVD PC mold (Figure 15a) and resulting PDMS neagtive stamp (Figure 15b) are depicted below.

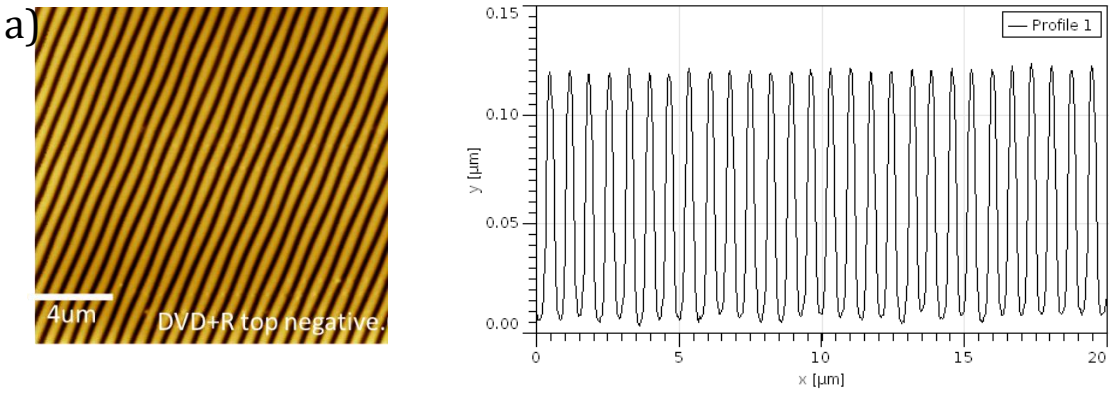

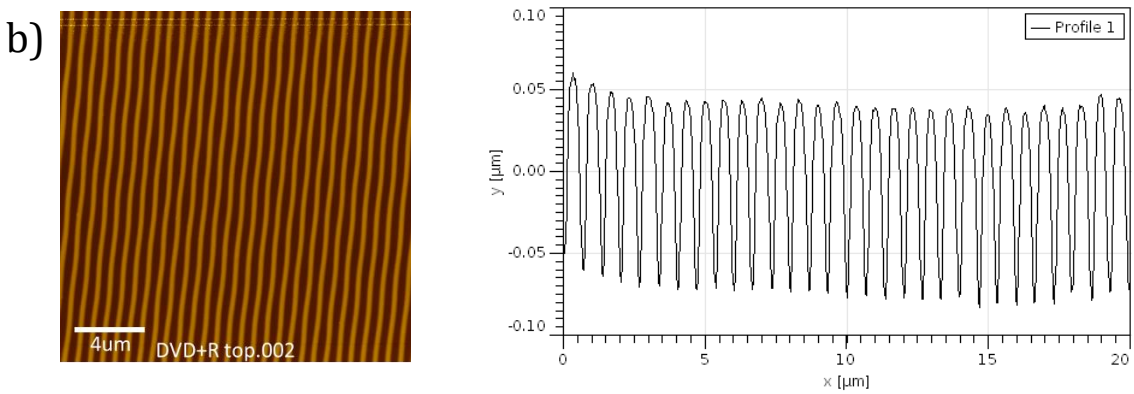

Figure 16: AFM micrograms of +R top a) DVD mold b) PDMS replica

The mean parameters of the DVD+R top patterns are: 290 ± 30 nm and spacing is 422 ± 19 and $113 \pm 2\,nm$.The depth of the negative PDMS stamp gratings are 119 ± 1nm. The deeper gratings on the PDMS may be caused by the elastic deformation during the lift-off process.
The schematic presentation of the DVD +R top part layers are depicted below (Figure 17).

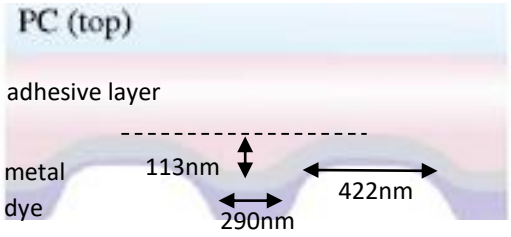

Figure 17: Schematic presentation of our sample of the PDMS mold

The DVD+R bottom parts have pits along the grooves which can be observed in the SEM images(Figure 18a). In the sample without azo (Figure 18b), the samples have no azo cover, thus the pits are more defined.

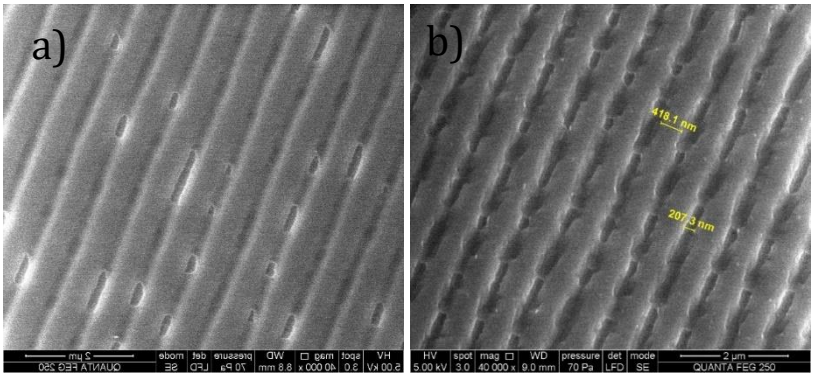

***Figure 18*:** DVD+R bottom : a) With Azo b) Without Azo

The mean parameters of the DVD+R bottom patterns are: periodicity of 554 ± 7 nm with spacing of 191 ± 15 and $113 \pm 2\ nm$. The data obtained from the AFM observations of DVD+R bottom surface topography are presented in the Figure 19.

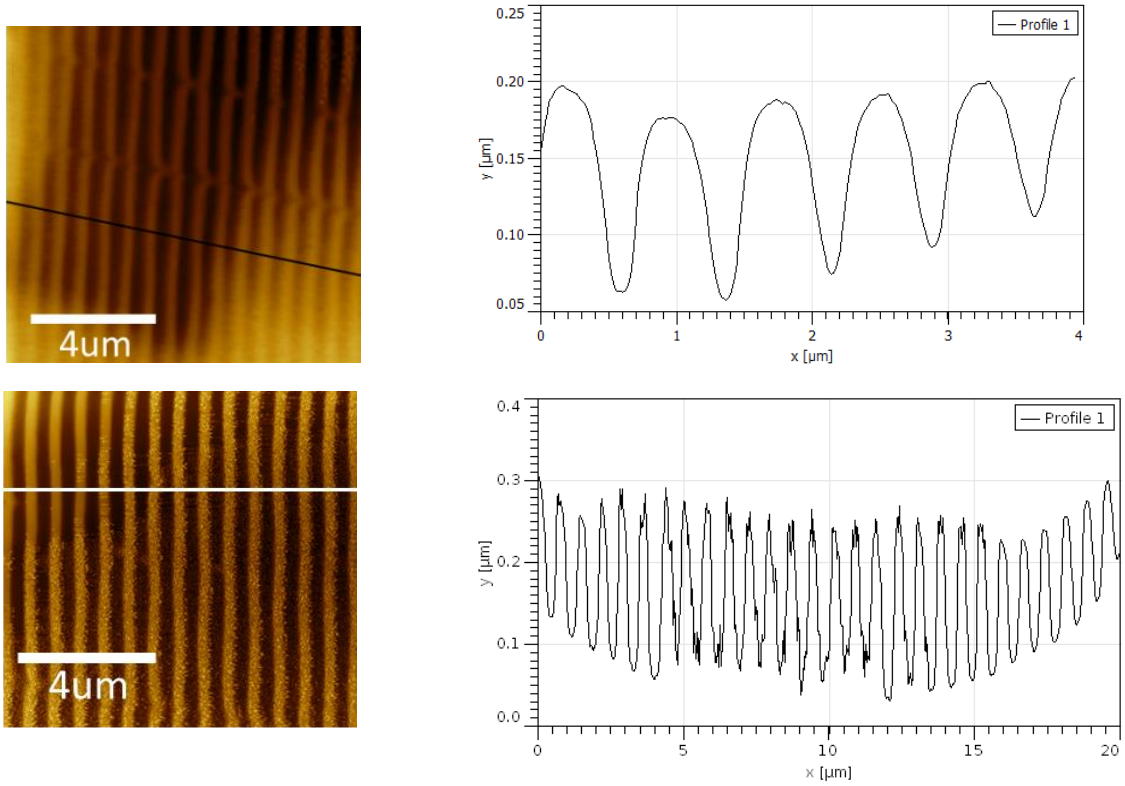

***Figure 19*:** PDMS negative of DVD+R bottom

4.4. Nanoimprinting on PVDF

The PVDF membrane has been used to check the effect of the temperature and pressure on the sample surface structure in terms of covering of the surface area by the pressed fibers. Compared to other floropolymers, PVDF has low melting point of around 171-177°C. The glass transition temperature is about -35°C and is typically 50-60% crystalline.

We compared the non-solvated PVDF hydrophobic membrane surface modifications, at hot embossing under varying conditions (time, temperature, pressure) presented in the Table 3 (Annex). The membranes were characterized by the SEM imaging.

5. Results and Discussion

5.1. Nanoimprinting on PVDF

The resulting degree of modification of the surface increased with the increasing temperature, time and the stamp profile. Even though the contact angles changed with the varying imprinting conditions, there is not much visible change (Figure 20).

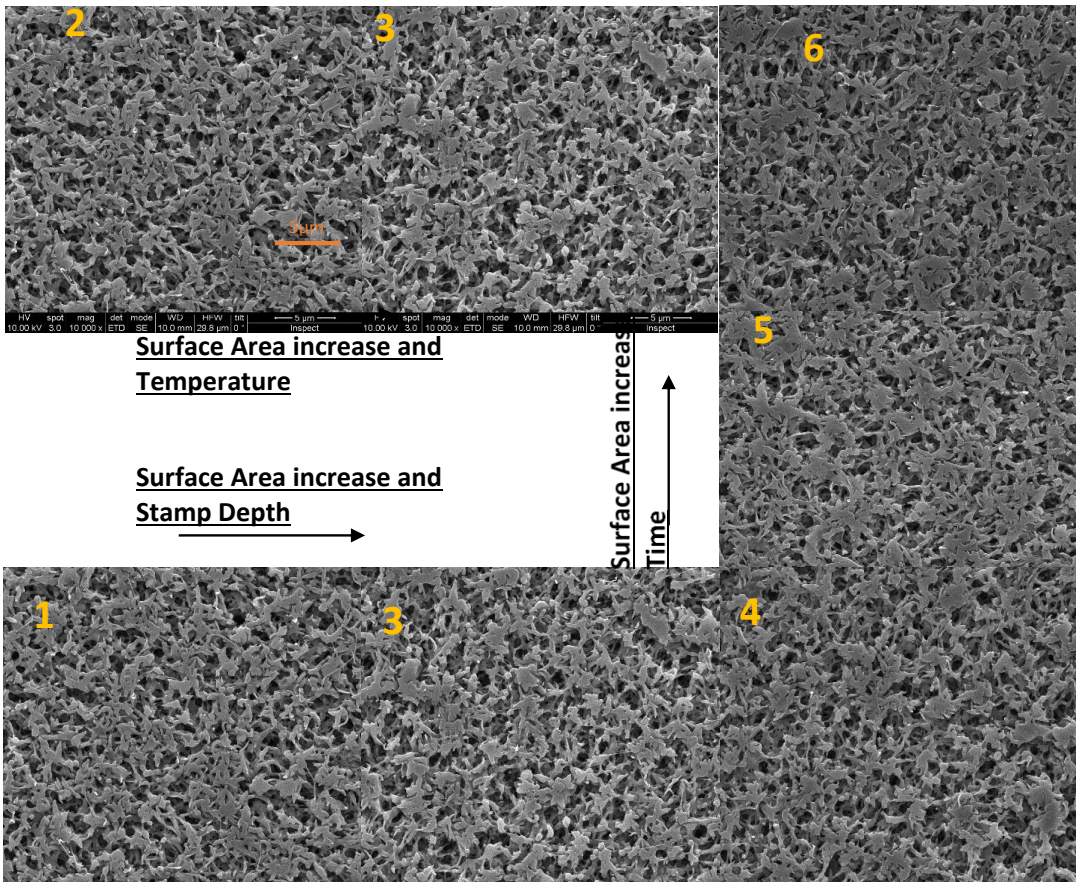

Figure 20: The PVDF samples ordered in terms of Temperature, time of imprinting and the depth of the stamp features

As can be from the Figure 11 the nanometric features won't be distinguished on the spong-like morphology of the surface, where the fibers and pores reach micrometer sizes. Thus the casted

dense PVDF would the suitable material for patterned replication. At the same time the material should pass liquid though it.

5.2. Future Work

Thus, the next strategy would be to fabricate the PVDF membranes with Phase separation technique, which results in smooth dense surface, separated by micron sized pores (Figure 21).

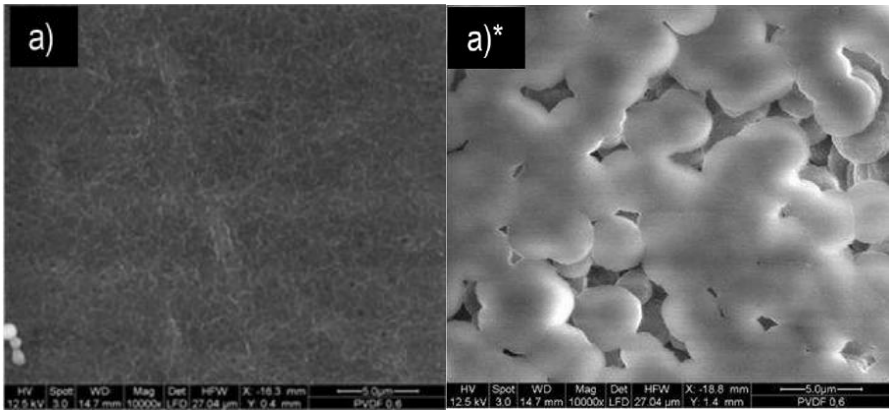

Figure 21: SEM images of the PVDF membrane surface magnify. X10000 [64]

The dense PVDF membrane fabricated by Drobek et al. [64] using phase inversion technique would be suitable for replication of the DVD patterns. As can be seen from the Figure 19 the flat surface area of at least 5μm are formed on the membrane surface, which is large enough for patterns of ~800 nm features.

Conclusions

Following research discusses the recent developments in membrane patterning techniques and their effect on different membrane processes.

Varying shapes and the sizes of the patterns results in distinct properties of the membranes. For filtration processes, depending on the size and shape, the patterns can vary physico-chemical interactions between the surface and foulants, as well as change the flow hydrodynamic at the surface. Patterning of the membranes for gas separation as well as PEM surfaces decrease the interfacial resistance and promotes better mass diffusion through them.

Patterning techniques vary by pattern replication resolution, fidelity and choice of patterned materials. This makes them applicable for some membranes and not applicable for others. Combining different techniques will open new prospects for larger applications. Finally having more advanced patterning techniques will enable designing complex plasmonic and optical nanostructures that will enable enhanced light-harvesting in the broad wavelength ranges.

[1] R. W. Baker, *Membrane Technology and Applications*. 2012.
[2] S. H. Maruf, A. R. Greenberg, J. Pellegrino, and Y. Ding, “Critical fl ux of surface-patterned ultra fi ltration membranes during cross- fl ow fi ltration of colloidal particles,” vol. 471, pp. 65–71, 2014, doi: 10.1016/j.memsci.2014.07.071.
[3] S. H. Maruf, L. Wang, A. R. Greenberg, J. Pellegrino, and Y. Ding, “Use of nanoimprinted surface patterns to mitigate colloidal deposition on ultrafiltration membranes,” *J. Memb. Sci.*, vol. 428, pp. 598–607, 2013, doi: 10.1016/j.memsci.2012.10.059.
[4] S. H. Maruf, A. R. Greenberg, J. Pellegrino, and Y. Ding, “Critical flux of surface-patterned ultrafiltration membranes during cross-flow filtration of colloidal particles,” *J. Memb. Sci.*, vol. 471, pp. 65–71, 2014, doi: 10.1016/j.memsci.2014.07.071.
[5] Y. Won *et al.*, “Factors affecting pattern fi delity and performance of a patterned membrane,” *J. Memb. Sci.*, vol. 462, pp. 1–8, 2014, doi: 10.1016/j.memsci.2014.03.012.
[6] S. Y. Jung, Y. J. Won, J. H. Jang, J. H. Yoo, K. H. Ahn, and C. H. Lee, “Particle deposition on the patterned membrane surface: Simulation and experiments,” *Desalination*, vol. 370, pp. 17–24, 2015, doi: 10.1016/j.desal.2015.05.014.
[7] S. H. Maruf *et al.*, “Influence of sub-micron surface patterns on the deposition of model proteins during active filtration,” *J. Memb. Sci.*, vol. 444, pp. 420–428, 2013, doi: 10.1016/j.memsci.2013.05.060.
[8] A. Al-Shimmery, S. Mazinani, J. Ji, Y. M. J. Chew, and D. Mattia, “3D printed composite membranes with enhanced anti-fouling behaviour,” *J. Memb. Sci.*, vol. 574, no. November 2018, pp. 76–85, 2019, doi: 10.1016/j.memsci.2018.12.058.
[9] Y. J. Won *et al.*, “Correlation of membrane fouling with topography of patterned membranes for water treatment,” *J. Memb. Sci.*, vol. 498, pp. 14–19, 2016, doi: 10.1016/j.memsci.2015.09.058.
[10] J. H. Jang *et al.*, “Correlation between particle deposition and the size ratio of particles to patterns in nano- and micro-patterned membrane filtration systems,” *Sep. Purif. Technol.*, vol. 156, pp. 608–616, 2015, doi: 10.1016/j.seppur.2015.10.056.
[11] O. Heinz, M. Aghajani, A. R. Greenberg, and Y. Ding, “ScienceDirect Surface-patterning of polymeric membranes : fabrication and performance,” pp. 1–12, 2018.
[12] Y. J. Won *et al.*, “Factors affecting pattern fidelity and performance of a patterned membrane,” *J. Memb. Sci.*, vol. 462, pp. 1–8, 2014, doi: 10.1016/j.memsci.2014.03.012.
[13] H. Yang and S. Wang, “A Review on the Effect of Microstructure Surface on the Adhesion of Marine Fouling Organisms,” *IOP Conf. Ser. Mater. Sci. Eng.*, vol. 782, no. 5, 2020, doi: 10.1088/1757-899X/782/5/052033.
[14] Y. Cheng, G. Feng, and C. I. Moraru, “Micro-and nanotopography sensitive bacterial attachment mechanisms: A review,” *Frontiers in Microbiology*, vol. 10, no. FEB. Frontiers Media S.A., p. 191, 21-Feb-2019, doi: 10.3389/fmicb.2019.00191.
[15] Y. J. Won *et al.*, “Preparation and application of patterned membranes for wastewater treatment,” *Environ. Sci. Technol.*, vol. 46, no. 20, pp. 11021–11027, 2012, doi: 10.1021/es3020309.
[16] O. Heinz, M. Aghajani, A. R. Greenberg, and Y. Ding, “Surface-patterning of polymeric membranes: fabrication and performance,” *Curr. Opin. Chem. Eng.*, vol. 20, pp. 1–12, 2018, doi: 10.1016/j.coche.2018.01.008.

[17] X. Zhu and M. Elimelech, “Colloidal fouling of reverse osmosis membranes: Measurements and fouling mechanisms,” *Environ. Sci. Technol.*, vol. 31, no. 12, pp. 3654–3662, 1997, doi: 10.1021/es970400v.
[18] Q. Li, Z. Xu, and I. Pinnau, “Fouling of reverse osmosis membranes by biopolymers in wastewater secondary effluent: Role of membrane surface properties and initial permeate flux,” *J. Memb. Sci.*, vol. 290, no. 1–2, pp. 173–181, 2007, doi: 10.1016/j.memsci.2006.12.027.
[19] A. Al-Amoudi and R. W. Lovitt, “Fouling strategies and the cleaning system of NF membranes and factors affecting cleaning efficiency,” *J. Memb. Sci.*, vol. 303, no. 1–2, pp. 4–28, 2007, doi: 10.1016/j.memsci.2007.06.002.
[20] E. M. Vrijenhoek, S. Hong, and M. Elimelech, “Influence of membrane surface properties on initial rate of colloidal fouling of reverse osmosis and nanofiltration membranes,” *J. Memb. Sci.*, vol. 188, no. 1, pp. 115–128, 2001, doi: 10.1016/S0376-7388(01)00376-3.
[21] I. M. A. ElSherbiny, A. S. G. Khalil, and M. Ulbricht, “Surface micro-patterning as a promising platform towards novel polyamide thin-film composite membranes of superior performance,” *J. Memb. Sci.*, vol. 529, no. June 2016, pp. 11–22, 2017, doi: 10.1016/j.memsci.2017.01.046.
[22] A. Malakian and S. M. Husson, “Understanding the roles of patterning and foulant chemistry on nanofiltration threshold flux,” *J. Memb. Sci.*, vol. 597, no. December 2019, 2020, doi: 10.1016/j.memsci.2019.117746.
[23] S. T. Weinman and S. M. Husson, “In fl uence of chemical coating combined with nanopatterning on alginate fouling during nano fi ltration,” vol. 513, pp. 146–154, 2016, doi: 10.1016/j.memsci.2016.04.025.
[24] M. Rickman, S. Maruf, E. Kujundzic, R. H. Davis, and A. Greenberg, “Fractionation and fl ux decline studies of surface-patterned nano fi ltration membranes using NaCl-glycerol-BSA solutions,” *J. Memb. Sci.*, vol. 527, no. January, pp. 102–110, 2017, doi: 10.1016/j.memsci.2017.01.007.
[25] I. M. A. Elsherbiny, A. S. G. Khalil, and M. Ulbricht, “Influence of surface micro-patterning and hydrogel coating on colloidal silica fouling of polyamide thin-film composite membranes,” *Membranes (Basel).*, vol. 9, no. 6, 2019, doi: 10.3390/membranes9060067.
[26] S. T. Weinman, E. M. Fierce, and S. M. Husson, “Nanopatterning commercial nanofiltration and reverse osmosis membranes,” *Sep. Purif. Technol.*, vol. 209, no. June 2018, pp. 646–657, 2019, doi: 10.1016/j.seppur.2018.09.012.
[27] J. A. Kharraz, M. R. Bilad, and H. A. Arafat, “Flux stabilization in membrane distillation desalination of seawater and brine using corrugated PVDF membranes,” *J. Memb. Sci.*, vol. 495, pp. 404–414, 2015, doi: 10.1016/j.memsci.2015.08.039.
[28] M. Breitwieser, M. Klingele, S. Vierrath, R. Zengerle, and S. Thiele, “Tailoring the Membrane-Electrode Interface in PEM Fuel Cells: A Review and Perspective on Novel Engineering Approaches,” *Adv. Energy Mater.*, vol. 8, no. 4, 2018, doi: 10.1002/aenm.201701257.
[29] S. Pawlowski, J. G. Crespo, and S. Velizarov, “Profiled ion exchange membranes: A comprehensible review,” *Int. J. Mol. Sci.*, vol. 20, no. 1, 2019, doi: 10.3390/ijms20010165.
[30] S. M. Kim *et al.*, “Prism-patterned Nafion membrane for enhanced water transport in polymer electrolyte membrane fuel cell,” *J. Power Sources*, vol. 317, pp. 19–24, 2016,

doi: 10.1016/j.jpowsour.2016.03.083.
[31] M. Aizawa, H. Gyoten, A. Salah, and X. Liu, “Pillar Structured Membranes for Suppressing Cathodic Concentration Overvoltage in PEMFCs at Elevated Temperature/Low Relative Humidity,” *J. Electrochem. Soc.*, vol. 157, no. 12, p. B1844, 2010, doi: 10.1149/1.3502613.
[32] M. Aizawa and H. Gyoten, “Effect of Micro-Patterned Membranes on the Cathode Performances for PEM Fuel Cells under Low Humidity,” *J. Electrochem. Soc.*, vol. 160, no. 4, pp. F417–F428, 2013, doi: 10.1149/2.085304jes.
[33] J. W. Bae, Y. H. Cho, Y. E. Sung, K. Shin, and J. Y. Jho, “Performance enhancement of polymer electrolyte membrane fuel cell by employing line-patterned Nafion membrane,” *J. Ind. Eng. Chem.*, vol. 18, no. 3, pp. 876–879, 2012, doi: 10.1016/j.jiec.2012.01.019.
[34] P. Izák, M. H. Godinho, P. Brogueira, J. L. Figueirinhas, and J. G. Crespo, “3D topography design of membranes for enhanced mass transport,” *J. Memb. Sci.*, vol. 321, no. 2, pp. 337–343, 2008, doi: 10.1016/j.memsci.2008.05.014.
[35] X. He, T. Wang, Y. Li, J. Chen, and J. Li, “Fabrication and characterization of micro-patterned PDMS composite membranes for enhanced ethanol recovery,” *J. Memb. Sci.*, vol. 563, no. April, pp. 447–459, 2018, doi: 10.1016/j.memsci.2018.06.015.
[36] J. Hee *et al.*, “Correlation between particle deposition and the size ratio of particles to patterns in nano- and micro-patterned membrane filtration systems,” *Sep. Purif. Technol.*, vol. 156, pp. 608–616, 2015, doi: 10.1016/j.seppur.2015.10.056.
[37] A. M. Peters, R. G. H. Lammertink, and M. Wessling, “Comparing flat and micro-patterned surfaces: Gas permeation and tensile stress measurements,” *J. Memb. Sci.*, vol. 320, no. 1–2, pp. 173–178, 2008, doi: 10.1016/j.memsci.2008.03.052.
[38] G. Firpo, E. Angeli, P. Guida, R. Lo Savio, L. Repetto, and U. Valbusa, “Gas permeation through rubbery polymer nano-corrugated membranes,” *Sci. Rep.*, vol. 8, no. 1, pp. 1–9, 2018, doi: 10.1038/s41598-018-24551-4.
[39] S. S. Ray, H. K. Lee, and Y. N. Kwon, *Review on blueprint of designing anti-wetting polymeric membrane surfaces for enhanced membrane distillation performance*, vol. 12, no. 1. 2020.
[40] L. Vogelaar *et al.*, “Phase separation micromolding: A new generic approach for microstructuring various materials,” *Small*, vol. 1, no. 6, pp. 645–655, 2005, doi: 10.1002/smll.200400128.
[41] Y. Gençal, E. N. Durmaz, and P. Z. Çulfaz-Emecen, “Preparation of patterned microfiltration membranes and their performance in crossflow yeast filtration,” *J. Memb. Sci.*, vol. 476, pp. 224–233, 2015, doi: 10.1016/j.memsci.2014.11.041.
[42] N. Izati *et al.*, “Development of a novel corrugated polyvinylidene difluoride membrane via improved imprinting technique for membrane distillation,” *Polymers (Basel).*, vol. 11, no. 5, pp. 1–13, 2019, doi: 10.3390/polym11050865.
[43] Q. Sun, Z. Yang, C. Hu, C. Li, G. Yan, and Z. Wang, “Facile preparation of superhydrophobic PVDF microporous membranes with excellent anti-fouling ability for vacuum membrane distillation,” *J. Memb. Sci.*, vol. 605, no. November 2019, p. 118106, 2020, doi: 10.1016/j.memsci.2020.118106.
[44] S. H. Maruf, Z. Li, J. A. Yoshimura, J. Xiao, A. R. Greenberg, and Y. Ding, “Influence of nanoimprint lithography on membrane structure and performance,” *Polymer (Guildf).*, vol. 69, pp. 129–137, 2015, doi: 10.1016/j.polymer.2015.05.049.

[45] S. T. Weinman and S. M. Husson, “Influence of chemical coating combined with nanopatterning on alginate fouling during nanofiltration,” *J. Memb. Sci.*, vol. 513, pp. 146–154, 2016, doi: 10.1016/j.memsci.2016.04.025.
[46] M. Xie, W. Luo, and S. R. Gray, “Surface pattern by nanoimprint for membrane fouling mitigation: Design, performance and mechanisms,” *Water Res.*, vol. 124, pp. 238–243, 2017, doi: 10.1016/j.watres.2017.07.057.
[47] S. H. Maruf, A. R. Greenberg, and Y. Ding, “Influence of substrate processing and interfacial polymerization conditions on the surface topography and permselective properties of surface-patterned thin-film composite membranes,” *J. Memb. Sci.*, vol. 512, pp. 50–60, 2016, doi: 10.1016/j.memsci.2016.04.003.
[48] J. Hutfles, W. Chapman, and J. Pellegrino, “Roll-to-roll nanoimprint lithography of ultrafiltration membrane,” *J. Appl. Polym. Sci.*, vol. 135, no. 11, pp. 1–12, 2018, doi: 10.1002/app.45993.
[49] N. U. Barambu, M. R. Bilad, Y. Wibisono, J. Jaafar, T. M. I. Mahlia, and A. L. Khan, “Membrane surface patterning as a fouling mitigation strategy in liquid filtration: A review,” *Polymers (Basel).*, vol. 11, no. 10, pp. 1–14, 2019, doi: 10.3390/polym11101687.
[50] Z. X. Low, Y. T. Chua, B. M. Ray, D. Mattia, I. S. Metcalfe, and D. A. Patterson, “Perspective on 3D printing of separation membranes and comparison to related unconventional fabrication techniques,” *J. Memb. Sci.*, vol. 523, pp. 596–613, 2017, doi: 10.1016/j.memsci.2016.10.006.
[51] G. Baffou and R. Quidant, “Thermo-plasmonics: Using metallic nanostructures as nano-sources of heat,” *Laser Photonics Rev.*, vol. 7, no. 2, pp. 171–187, 2013, doi: 10.1002/lpor.201200003.
[52] L. De Sio *et al.*, “Next-generation thermo-plasmonic technologies and plasmonic nanoparticles in optoelectronics,” *Prog. Quantum Electron.*, vol. 41, pp. 23–70, 2015, doi: 10.1016/j.pquantelec.2015.03.001.
[53] J. Frischeisen *et al.*, “Light extraction from surface plasmons and waveguide modes in an organic light-emitting layer by nanoimprinted gratings,” *Opt. Express*, vol. 19, no. S1, p. A7, 2011, doi: 10.1364/oe.19.0000a7.
[54] A. Sierant, R. Panaś, J. Fiutowski, H. G. Rubahn, and T. Kawalec, “Tailoring optical discs for surface plasmon polaritons generation,” *Nanotechnology*, vol. 31, no. 2, 2020, doi: 10.1088/1361-6528/ab4688.
[55] D. Agarwal *et al.*, “Engineering Localized Surface Plasmon Interactions in Gold by Silicon Nanowire for Enhanced Heating and Photocatalysis,” *Nano Lett.*, vol. 17, no. 3, pp. 1839–1845, 2017, doi: 10.1021/acs.nanolett.6b05147.
[56] L. D. Tijing, Y. C. Woo, J. S. Choi, S. Lee, S. H. Kim, and H. K. Shon, “Fouling and its control in membrane distillation-A review,” *J. Memb. Sci.*, vol. 475, pp. 215–244, 2015, doi: 10.1016/j.memsci.2014.09.042.
[57] J. A. Kharraz, M. U. Farid, N. K. Khanzada, B. J. Deka, H. A. Arafat, and A. K. An, “Macro-corrugated and nano-patterned hierarchically structured superomniphobic membrane for treatment of low surface tension oily wastewater by membrane distillation,” *Water Res.*, vol. 174, pp. 1–15, 2020, doi: 10.1016/j.watres.2020.115600.
[58] M. A. Khan, L. Sinatra, M. Oufi, O. M. Bakr, and H. Idriss, “Evidence of Plasmonic Induced Photocatalytic Hydrogen Production on Pd/TiO2 Upon Deposition on Thin Films of Gold,”

Catal. Letters, vol. 147, no. 4, pp. 811–820, 2017, doi: 10.1007/s10562-017-1998-4.
[59] L. García-Fernández, C. García-Payo, and M. Khayet, "Hollow fiber membranes with different external corrugated surfaces for desalination by membrane distillation," *Appl. Surf. Sci.*, vol. 416, pp. 932–946, 2017, doi: 10.1016/j.apsusc.2017.04.232.
[60] J. A. Kharraz and A. K. An, "Patterned superhydrophobic polyvinylidene fluoride (PVDF) membranes for membrane distillation: Enhanced flux with improved fouling and wetting resistance," *J. Memb. Sci.*, vol. 595, no. July 2019, 2020, doi: 10.1016/j.memsci.2019.117596.
[61] Z. Xiao *et al.*, "Slippery for scaling resistance in membrane distillation: A novel porous micropillared superhydrophobic surface," *Water Res.*, vol. 155, pp. 152–161, 2019, doi: 10.1016/j.watres.2019.01.036.
[62] J. U. Kim, S. Lee, S. J. Kang, and T. Il Kim, "Materials and design of nanostructured broadband light absorbers for advanced light-to-heat conversion," *Nanoscale*, vol. 10, no. 46, pp. 21555–21574, 2018, doi: 10.1039/c8nr06024j.
[63] A. Politano *et al.*, "Photothermal Membrane Distillation for Seawater Desalination," *Adv. Mater.*, vol. 29, no. 2, 2017, doi: 10.1002/adma.201603504.
[64] M. Drobek *et al.*, "PVDF-MFI mixed matrix membranes as VOCs adsorbers," *Microporous Mesoporous Mater.*, vol. 207, pp. 126–133, 2015, doi: 10.1016/j.micromeso.2015.01.005.
[65] S. H. Maruf, A. R. Greenberg, J. Pellegrino, and Y. Ding, "Fabrication and characterization of a surface-patterned thin film composite membrane," *J. Memb. Sci.*, vol. 452, pp. 11–19, 2014, doi: 10.1016/j.memsci.2013.10.017.

ANNEX

Table 1: Fabricating conditions of TFC membranes and UF supports

	Stamp dimensions /Fidelity (%)	**UF support /TFC patterning conditions**	**Performance changes in UF support**	**Performance changes in TFC**	**Ref.**
UF PES support	p/w/d = 575/ 210/ 180 nm Fidelity =~ 67%	120 _C 40 bars 3 min	10% decline in DI water permeation	-	[44]
TFC micropatterned MIL (PES support) Interfacial polimerization (IP) of PA	d/p = ~10-20µm Fidelity l/w = 50% d = 20% roughness =276nm	MIL at 10 bar, 110 °C 35 min	-	Salt 10000 concentration Slight increase in rejection-96% 10% decline in permeability vs flat	[21]
TFC micropatterned PSµM (PES support) and IP of PA	~10-20µm l/w=70% d= 50% roughness = 492	VIPS + NIPS	-	10% higher permeability and higher salt rejection 21% decline in permeability	[21]
TFC nanopatterned UF PES support + IP of PA	p/d = 834/ 200 nm printed UF d =100–120nm TFC ~50nm depth	120 °C 40 bars 3 min	Stirred flux decline 12%_unpatterned 8% - patterned Salt rejection decline 13% -unpatterned 9% - patterned	40% lower permeance than Dow_NF_270 12% decline from non-patterned	[65]
TFC commercial Dow_NF_270 directly NIL imprinted	Mold d/w = 190 /~600nm Fidelity ~75%	189 ± 38 bar 45 °C 20 min	-	DI water permeance 22% lower than commercial unpatterned 15% decline in $MgSO^4$ rejection possible fracturing Most of the other RO -no change in rejection 92% rejection	[45]

Table 2: Comparison of different treatments of the MD membranes [27], [57], [60]

Modification	Experiment time	Flux decline with high surf. tension liquids	Flux decline from low surface tension liquids	Contact angle/Sliding angle
Commercial hydrophobic PVDF	3mins	-	oil conc. 50 ppm 100%	DW -123.1 ^{o} ± 1.5 5mM SDS -82.7 ± 2.1 after 3min s- 70.5 ± 1.6 sliding ^{o} = >90 ^{o}
SCM Superhydrophobic Corrugated Membrane	2h	-	oil conc. at 100 ppm conc 25% drop at 200 ppm oil conc. 40% drop	DW 152.4 ^{o} ± 2.3 SDS - 143.1 ^{o} ± 1.9 Eth. - 23.6 ^{o} sliding ^{o} = 22.4 ^{o} +-3.2
SOM Super Omniophobic Membrane	24h	-	oil 400 ppm stable flux	DW-160.8 ± 2.3 oil- 154.3 ± 1.9 SDS-148.3 ± 1.6 eth - 118.7 ± 2.2 sliding ^{o} = 3.8+-1.3
Modification/Chemical treatment	Time	Flux decline high surf. Tension liquids	Flux decline from low surface tension liquids	Contact angle /sliding angle
C-PVDF Commercial membrane	97h	complete fouling - 100%	fouled at < 0.1mM wetting	SDS before filtration /after filtration - 82.7/18.9
PM Patterned membrane	133h	18.35% drop	fouled at > 0.3mM	SDS - 119 ^{o} /117 ^{o}
	97h	13.9% \(from 23 to 19.8 LMH)		
SPM Superhydrophobic patterned membrane (patterned and chemically treated)	97h	13.60%	resistant to> 0.4mM	SDS - 143.1 ^{o} /122 ^{o}
	133h	19.60%		

SEM and AFM characterization: DVD -R

The top part of DVD-R have a regular periodical structure without defects with pitch of $210 \pm 40nm$ and groove of $490 \pm 30nm$ (Annex Table 7,8).

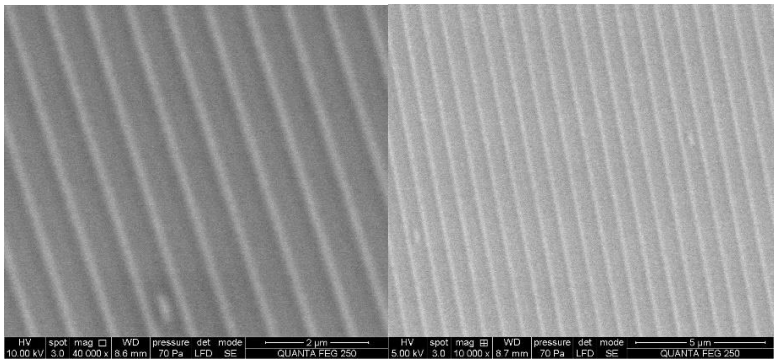

Figure 1: *DVD-R top parts b) no Al c) with Al*

The DVD-R bottom part has a continuous periodical structure (Figure 2), with the pitch of $510 \pm 30nm$ and groove of $200 \pm 30nm$.

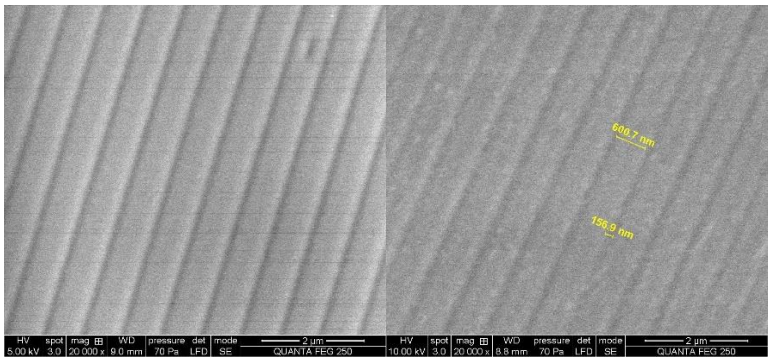

Figure 2: *DVD-R bottom , a) no Al b) with Al*

The AFM observations of the DVD-R bottom pure PC layer is shown below (Figure3). The measured mean depth of PC bottom layer grooves is $38 \pm 3nm$. The gratings on the PDMS negative of this sample were less deep: $31 \pm 2nm$. This depth is rather shallow than the grating depth in the DVD+R(113-190nm). Therefore, only the top DVD-R part has been used as a PDMS mold.

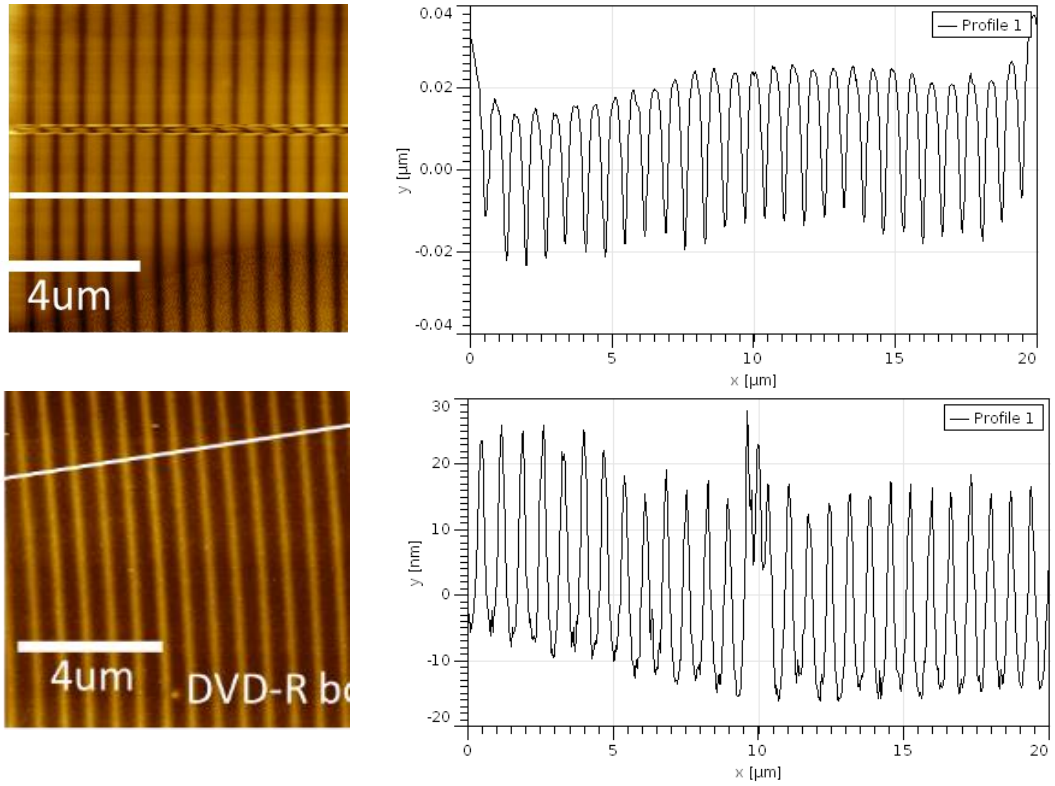

Figure 3: a) DVD-R bottom PC layer and b) PDMS negative of DVD -R bottom

The mean dimensions of the DVD -R bottom patterns are $510 \pm 30nm$ and groove of $200 \pm 30n$ *and* the depth of $38 \pm 3nm$.

Table 3: PVDF samples and the resulting modifications of the surfaces

Sample Name	Temperature (T) (°C)	Pressure (bars)	Time pressed (min)	Release T (°C)	The relative area of the pressed fibers (%)
Sample 1	150	8	10	60	43.6
Sample 2	135	8	15	60	51.7
Sample 3	150	8	10	60	53.6
Sample 4	145	8	10	60	53.9
Sample 5	165	8	5	60	48.2
Sample 6	165	8	10	60	55

Table 4: SEM and AFM measurements of DVD+R top and PDMS surfaces

Width (um)	Mean	STD Dev	Spacing (um)	Mean	STD Dev
271,337	290.671	26.884	412,012	421.812	19.274
336,028			433.664		
271,337			395.478		
292,969			445.381		
281,684			422.526		
Depth (um)	**Mean**	**STD Dev**	**PDMS_depth**	**mean**	**STD dev**
114	113.333	2.1	117.753	118.95	1.0
115			119.358		
111			120.164		
			118.559		

Table 5: SEM and AFM measurements of DVD+R bottom surfaces

width (nm)	mean	STD dev	spacing (nm)	mean	STD dev
563.65	553.49	7.27	201.12	190.6233	14.72
547.11			201.12		
554.72			170.38		
556.17			179.36		
545.81			201.12		

Table 6: AFM measurements of PDMS replica of DVD+R bottom surface

Depth_PDMS	Mean	STD dev
215	197	18.078
220		
183		
179		
182		

Table 7: SEM measurements of DVD-R top and PDMS surfaces

Spacing (nm)	mean	STD dev	Width	mean	STD dev
492.443	493.7364	25.14062	269.258	207.2227	36.57527
469.707			210.9766		
514.782			188.0559		
523.2341			188.0559		
468.5157			179.7674		

Table 8: SEM and AFM measurements of DVD-R bottom and PDMS surfaces

Spacing (nm) -R bottom	mean	STD dev	Width (nm) -R Bottom	Mean	STD dev
230.489	200.2	30	501	514	30
206.155			475		
158.114			550		
206.155			530.33		
Depth (nm) DVD -R bottom	**Mean**	**STD dev**	**Depth (nm) PDMS -R bottom**	**mean**	**STD dev**
34.29	37.77446	3.38	34.11	31.17	2.04
35.43			29.32		
42.87			29.73		
37.15			32.47		
39.14			30.28		